Research Article

Carbon aerogel reinforced PDMS nanocomposites with controllable and hierarchical microstructures for multifunctional wearable devices

Yan Sun [a], Deping Li [b], Jong Uk Kim [c], Bing Li [d], Seung-Hyun Cho [a], Tae-il Kim [c], Jae-Do Nam [a, e], Lijie Ci [b, f], Jonghwan Suhr [a, e, g, *]

[a] Department of Energy Science, Sungkyunkwan University, Suwon, 440-746, South Korea
[b] School of Materials Science and Engineering, Harbin Institute of Technology, Shenzhen, 518055, Guangdong, China
[c] School of Chemical Engineering, Sungkyunkwan University, Suwon, 440-746, South Korea
[d] Department of Materials Science and Engineering, Korea Advanced Institute of Science and Technology, Daejeon, 34141, South Korea
[e] Department of Polymer Science and Engineering, Sungkyunkwan University, Suwon, 440-746, South Korea
[f] Key Laboratory for Liquid-Solid Structural Evolution & Processing of Materials (Ministry of Education), School of Materials Science and Engineering, Shandong University, Jinan, 250061, China
[g] School of Mechanical Engineering, Sungkyunkwan University, Suwon, 440-746, South Korea

ARTICLE INFO

ABSTRACT

Wearable devices have attracted increasing attention for development of personal healthcare. In this study, three-dimensional porous carbon aerogels reinforced polydimethylsiloxane nanocomposites with controllable and hierarchical open, semi-open and closed cell structures were developed for multifunctional wearable heating and sensing devices. This investigation reveals that the microstructures of the aerogels play a critical role in determining nanocomposites properties, particularly their heating and sensing performances. As thermotherapy heaters, the nanocomposite with semi-open cell structure is observed with the highest energy transduction efficiency (equilibrium temperature ~138.9 °C under only 5 V) compared to the nanocomposites with open and closed cell structures, due to the well-defined conductive network and structural stability. As stimuli-responsive sensors, compared to the nanocomposite with closed cell structure, the nanocomposites with open and semi-open cell structures are observed with higher sensitivity (gauge factor ~369.03) and much better repeatability, benefiting from their structural integrity. Finally, the nanocomposite with semi-open cell structure was investigated for practical potential on human body. Experimental results demonstrated the uniform temperature distribution and reliable sensitivity as a multifunctional wearable device. Therefore, by controlling and optimizing the microstructure of carbon aerogels, the nanocomposites with tailored microstructure could be exploited for various engineering applications including emerging multifunctional wearable devices.

© 2020 Elsevier Ltd. All rights reserved.

1. Introduction

Wearable devices, or wearable technology are labeled as the next frontier in personalized healthcare [1–3], as they are playing an evolutionary role from monitoring fitness to improving diagnosis and healthcare. For example, a wearable thermotherapy heater device can provide pain relief and enable efficient repair of muscle fibers due to the increase of blood flow and oxygen delivery to cells [4,5]. The temperature can be easily controlled through the conversion of electric energy into heat energy. In addition, wearable body motion detectors based on the stimuli-responsive sensing capability are also widely used for entertainment technology, fitness tracking, and personal healthcare monitoring [6,7]. Nowadays, the integration of multifunctionality has become one of the most attractive attributes for the emerging wearable healthcare devices. Thus, it seems to be highly desirable to develop a multifunctional device with both heating and sensing capabilities in one material system. Despite the extensive studies on the

* Corresponding author. Department of Energy Science, Sungkyunkwan University, Suwon, 440-746, South Korea.
  E-mail address: suhr@skku.edu (J. Suhr).

thermotherapy heaters or body motion detectors, only few devices have been investigated with their multifunctionality [8,9]. In addition, these multifunctional devices do not seem to work well enough due to the high-power utilization, insufficient reliability, and scarce wearability [10–13], which make it particularly important to develop the wearable heater/sensor devices that require low power consumption, long-term stability as well as the enhanced wearability.

One of the feasible ways to improve the wearability is to transform the rigid device into a flexible one, so it can still maintain the high performance while experiencing large mechanical deformations following the human body motions. Poly-dimethylsiloxane (PDMS) is widely used for flexible electronics due to excellent flexibility, biocompatibility, and high thermal stability. A number of studies have reported on the PDMS-based flexible devices by coating or printing a conductive layer onto the flexible PDMS substrate [14,15]. However, the main challenges of this approach are found to be the weak adhesion [16] and the mechanical incompatibility [1], which could cause the structural failure of the devices under large deformation. Another approach to develop PDMS-based flexible devices is to disperse electrically conductive fillers inside the PDMS matrix. However, it requires higher loading fractions of the conductive fillers to achieve high enough electrical conductivity, which then often results in the high viscosity and, as a consequence, inhomogeneous dispersion of the fillers [17]. To address these issues, the exploitation of three-dimensional (3D) porous carbon aerogels as the reinforcement of PDMS is considered as one effective way to achieve the high electrical conductivity with high structural stability [18].

Herein, the 3D conductive porous carbon reinforced PDMS nanocomposites were developed for the multifunctional wearable devices in this study. Different from the previously reported nanocomposites reinforced by the carbon aerogels with only one porous structure [8,19,20] or just varying the cell size/wall thickness [21], the carbon aerogels with controllable microstructures including hierarchical open, semi-open and closed cell structures are designed and synthesized in this work. To optimize the PDMS nanocomposites for reliable wearable performance, the microstructure-composite property relationship was systemically investigated, including the composites structural morphology, electrical conductivity, and structural stability, etc. To the best of our knowledge, this is the first report to investigate the relationship between the microstructures of the carbon aerogels with hierarchical open, semi-open or closed cell structures and the properties of the nanocomposites with multiple functions, which could provide useful insights and design guidelines for newly developing 3D porous architecture reinforced nanocomposites.

To further evaluate the effect of the microstructures on the device performances, the heating performance was firstly investigated for the nanocomposites to work as a thermotherapy heater. It was experimentally demonstrated with the considerably lower power consumption for the nanocomposite with semi-open cell structure compared to previously reported materials [8,9,14–17], due to the well-defined conductive network and structural stability. The outstanding stability of the flexible heater device is also confirmed by conducting the cyclic bending-unbending deformations for more than 12,000 cycles, benefiting from the high structural integrity. More than working as heater devices, the nanocomposites were also evaluated as stimuli-responsive sensors under different tensile, compressive and bending deformations, with the primary focus being to investigate the impact of the microstructures on the sensing performance. The nanocomposites with open and semi-open cell structures were observed to have a higher sensitivity with much better repeatability under different deformation modes, due to the higher structural integrity over the

nanocomposite with closed cell structure. Finally, the potential use for practical applications of the multifunctional device was examined on the wrist and under the heel, respectively in order to evaluate the heat-generation and body motion detecting capabilities. The results of this study could indicate that by controlling the microstructures of the carbon aerogels, the porous carbon aerogel reinforced PDMS nanocomposites with tailored microstructure could show great potential for the use as multifunctional wearable heating and sensing devices.

2. Experimental

2.1. Materials

Graphene Oxide (GO) powder was supplied by JW-Innova Graphene Technology Co., LTD. Poly(vinyl alcohol) (PVA, Mw 85,000–124,000, 87%–89% hydrolyzed) was obtained from Sigma-Aldrich. Formaldehyde solution (FA, 37 wt% in H_2O) and hexane were purchased from Daejung Chemical &Materials Co., LTD. PDMS (sylgard 170, part A&B) was provided by Dow Corning. All materials were used without further treatment.

2.2. Preparation of hierarchical porous carbon

The experimental scheme is shown in Fig. 1a. Firstly, GO-PVA-FA (GPF) aerogels with hierarchical porous structures were synthesized with GO, PVA, and FA by the two-step crosslinking reaction as introduced in our previous work [22,23]. Specifically, GO solutions with three different loading fractions were dispersed in water by bath sonication for 6 h and PVA solution (9 wt%) was prepared by stirring in the water at 90 °C for 6 h. GO solution was mixed with PVA solution under stirring at 50 °C for 2 h. After that, FA solution was added at 85 wt% of PVA and stirred for another 2 h to get the GPF solution. GPF aerogels were obtained after the further reaction of the GPF solutions in the oven at 50 °C for 16 h followed by freeze-drying at −84 °C for 48 h. According to the loading fraction of GO (20 wt%, 40 wt%, and 60 wt% out of PVA and FA weight in total), GPF aerogels prepared were named as GPF1, GPF2, and GPF3, respectively. Finally, GPF aerogels were annealed at 900 °C for 2 h under argon atmosphere for the thermal reduction. The electrically conductive aerogels with hierarchical porous structures obtained from the annealed GPF1, GPF2, and GPF3 aerogels were labeled as anGPF1, anGPF2, and anGPF3, respectively.

2.3. Preparation of anGPF-PDMS nanocomposites

Part A of PDMS resin (Sylgard 170) was mixed with hexane in a mass ratio of 2:1 by vigorously stirring for 5 min to reduce the viscosity of the polymer matrix. Then, part B of PDMS resin (Sylgard 170) was added at 1:1 mass ratio of part A and mixed at 2000 rpm for 2 min followed by defoaming at 2200 rpm for another 2 min using a shear mixer. The diluted matrix mixture was then poured into a plastic petri dish where the annealed GPF aerogels were placed. After putting the samples inside a vacuum chamber for around 1 h, the air bubbles would be removed and the PDMS matrix would be infiltrated into the carbon aerogels. Finally, the nanocomposites were obtained after curing the infiltrated PDMS at 50 °C for 12 h. The nanocomposites prepared with different anGPF aerogels were labeled as anGPF1-PDMS, anGPF2-PDMS, and anGPF3-PDMS, respectively. To fabricate the device, anGPF-PDMS nanocomposites were cut into desired rectangle shapes, and sliver wires were attached on both sides of the nanocomposite with silver paste followed by curing at 50 °C for 12 h.
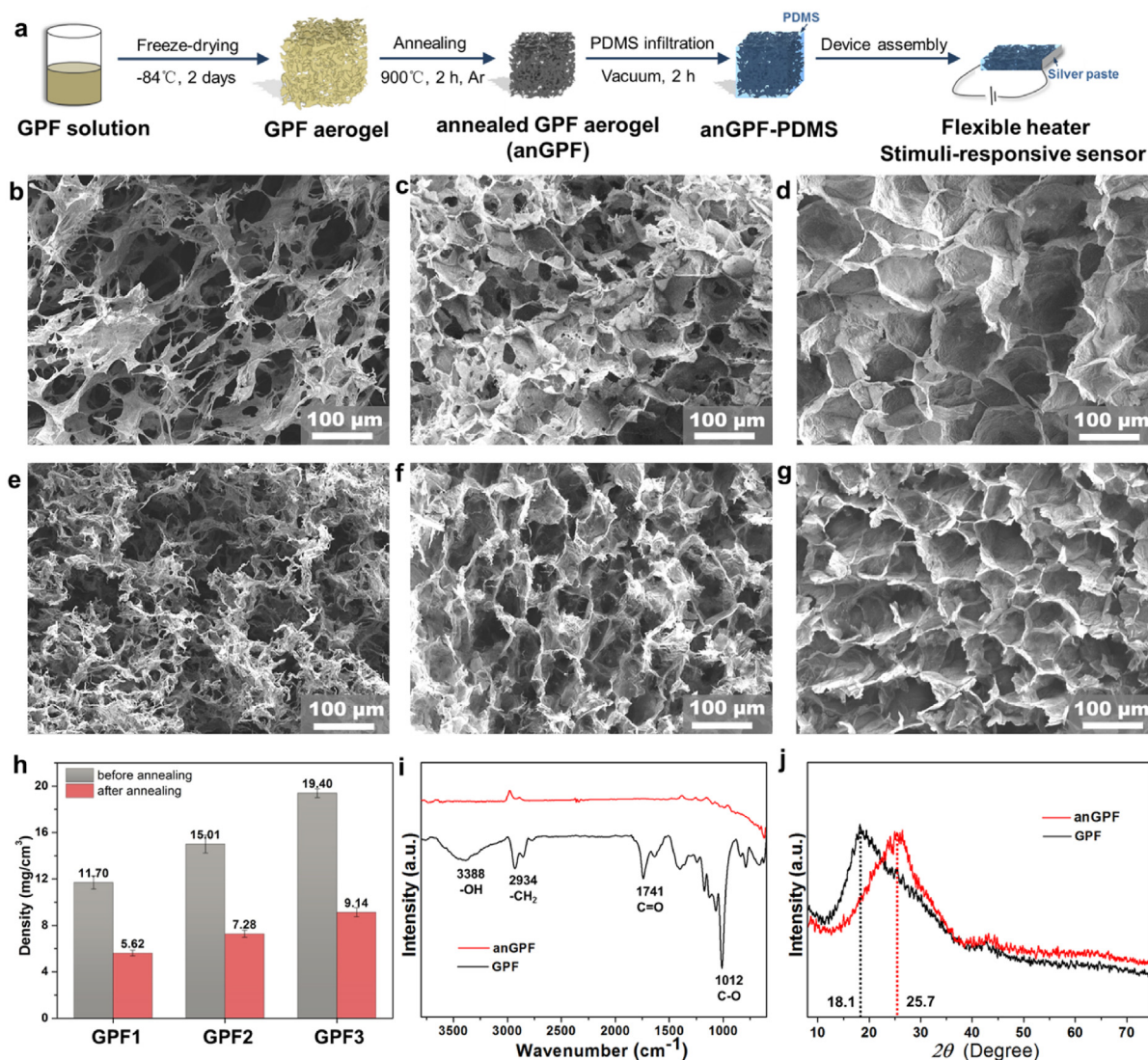
Fig. 1. a, Synthesis scheme for fabrication of anGPF-PDMS nanocomposites and assembly of the multifunctional wearable device with anGPF-PDMS nanocomposite. b-d, SEM images of GPF1, GPF2 and GPF3, respectively. e-g, SEM images of anGPF1, anGPF2 and anGPF3, respectively. h, Densities of GPF1, GPF2, GPF3 aerogels before and after annealing. i and j, FTIR spectra and XRD patterns of GPF2 aerogel and anGPF2 aerogel, respectively. (A colour version of this figure can be viewed online.)

2.4. Characterization

The structural morphologies of GPF aerogels, anGPF aerogels, and anGPF-PDMS nanocomposites were characterized using a field emission scanning electron microscope (FE-SEM, JSM-7600F, JEOL) at an acceleration voltage of 10 kV. The element mapping and relative element content were collected with energy dispersive spectroscopy during the SEM investigation (SEM-EDS). X-ray diffraction analysis (XRD, Cu-Kα radiation, SmartLab) was performed for GPF and anGPF aerogels to check the inter-layer distance. FTIR spectra of GPF and anGPF aerogels were recorded using an attenuated total reflection infrared spectrometer (ATR-IR, Tensor 27, Bruker, Germany) from 400 to 4000 cm^{-1} at a resolution of 4 cm^{-1} with 50 scans. Raman spectra of GPF and anGPF aerogels were determined at 532 nm laser wavelength equipped with optical microscopy (RENISHAW, inVia). All mechanical tests were performed using the universal test machine (ElectroPuls E3000 Testing System, Instron) equipped with a 250 N load cell. For the heater performance testing, the temperature was recorded with a digital multimeter (Agilent, 34411A) equipped with a 10 kΩ

thermistor. Infrared temperature images were taken with an infrared camera (FLIR, T600). During the stimuli-responsive sensing testing, the deformation was generated and controlled by using the universal test machine, and the resistance was recorded with the digital multimeter (Agilent, 34411A) by a two-probe method.

3. Results and discussion

3.1. Characterization of carbon aerogels

SEM images are taken to investigate the structural morphologies of both GPF and annealed GPF aerogels with different GO loading fractions (Fig. 1b–g). As shown in Fig. 1b, GPF1 has an open cell porous structure with pore diameter widely scattered from 10 to 100 μm, while GPF2 (Fig. 1c) is observed to have the cellular structure with the cell diameters of around 70 μm. It should be noted that the cells of GPF2 are found to be not completely closed but with some holes through the cell walls as the inter-pore passages, ultimately making the internal microstructure of GPF2 aerogels as a semi-open cell network. As the loading fraction of GO is

increased to 60%, GPF3 (Fig. 1d) becomes a well-connected cellular structure with almost nearly closed cell walls and the average cell diameter is measured to be around 100 μm anGPF aerogels, which are named for GPF aerogels after annealing, are also found to have the hierarchical internal structures with the increase of the GO loading fraction, just similar to GPF aerogels. anGPF1 (Fig. 1e) is observed to possess the open cell porous structure with the scattered pore size ranging from several nanometers to 20 μm. In contrast to the planar sheets seen inGPF1, more curled and shrunk branches are observed in anGPF1. For anGPF2 (Fig. 1f), the internal microstructure becomes a semi-open cell cellular network with the pore diameters ranging from 30 to 70 μm. Similar to GPF3, anGPF3 (Fig. 1g) is found to have a well-connected cellular structure with nearly closed cell pores and the pore size is measured to be around 85 μm. Compared to GPF aerogels, the corresponding anGPF aerogels are observed to possess smaller pore diameters, resulting from the elimination of functional groups and the shrinkage of interlayer distance after thermal reduction. The structural morphology characterization results could indicate that the porous structures of both GPF and anGPF aerogels are able to be controlled quite effectively by simply varying the loading fraction of GO. The integrity of cell walls on the porous carbon network becomes greater as the GO loading fraction increases, which correspondingly contributes to the transition of GPF and anGPF aerogels from the randomly disordered open cell to semi-open cell and eventually the nearly closed cell structures.

Bulk densities are measured for the hierarchical carbon aerogels. As shown in Fig. 1h, the densities increase from GPF1 to GPF3 (11.70–19.40 mg cm^{-3}) as the loading fraction of GO increases. The density of anGPF aerogels is measured to be smaller than the half value of the corresponding GPF aerogels (5.62–9.14 mg cm^{-3}), indicating the ultra-lightweight of anGPF aerogels after annealing. The dramatic decrease in the bulk density for anGPF aerogels could be attributed to the removal of functional groups of GPF aerogels during the annealing process. FTIR and XRD spectra are recorded and characterized for both GPF and anGPF aerogels (note GPF2 and anGPF2 are shown as representative). As shown in Fig. 1i, the FTIR spectra of GPF aerogels contain the peaks at 3338, 2934, 1741, and 1012 cm^{-1}, corresponding to the vibration peaks of O-H, CH$_2$, C=O, and C-O, respectively. However, almost all functional groups are shown to be removed after annealing at 900 °C for 2 h, ensuring the successful thermal reduction of GPF aerogels. In addition, some of the sp^2 hybridized C-C bonds might be also broken, consequently resulting in the increase of the amorphous sp^3 carbons, which is supported by the Raman spectra (Fig. S1a), showing the increase of I$_D$/I$_G$ ratio from 0.73 of GPF aerogel to 1.18 of anGPF aerogel. The XRD patterns of GPF and anGPF aerogels are shown in Fig. 1j. Compared to the 2θ (18.1°) of GPF aerogels, the increased value (25.7°) of anGPF aerogels indicates a decrease of the interlayer distance according to Bragg's law, which would be attributed to the removal of oxygen-containing groups on the carbon basal plane during the thermal reduction.

3.2. Effect of porous structure on nanocomposites properties

Having captured the microstructures of three different anGPF aerogels with varied GO loading fractions, the effects of the hierarchical structures on the properties of corresponding nanocomposites are investigated. Firstly, SEM images were examined to investigate the internal morphologies of anGPF-PDMS nanocomposites. As shown in Fig. 2a, no obvious void is observed in anGPF1-PDMS, indicating its high structural integrity. However, the carbon network of anGPF1 aerogel is shown to be broken, turning to a non-continuous microstructure in PDMS matrix. In contrast, the SEM image of anGPF2-PDMS (Fig. 2b) indicates that anGPF2

aerogel can maintain the well-defined cellular structure in PDMS matrix with the pore size around 70 μm and without any noticeable voids. Thus, it can be believed that a continuous conductive network is well-developed and formed in anGPF2-PDMS with high structural integrity. However, anGPF3-PDMS exhibits plenty of large voids with the size around 85 μm (Fig. 2c). The different morphologies of anGPF-PDMS nanocomposites could be attributed to the microstructures of anGPF aerogels. Due to the high viscosity of the PDMS matrix (~2135 cp), the open or semi-open cell structures of anGPF1 and anGPF2 aerogels could provide a large enough pathway for the polymer fluid to penetrate through the porous structure. However, the nearly closed cell structure of anGPF3 could induce greater fluid-flow resistance, making it far more difficult for the PDMS to be infiltrated into the pores. Thus, anGPF1-PDMS and anGPF2-PDMS nanocomposites are confirmed with higher structural integrity, while plenty of large voids are found in anGPF3-PDMS nanocomposites.

After characterization of the microstructures, bulk density and electrical conductivity of anGPF- PDMS nanocomposites were further measured to investigate the influence of hierarchical microstructure on the nanocomposites properties. The densities (Fig. 2d) of neat PDMS, anGPF1-PDMS, anGPF2-PDMS, and anGPF3-PDMS are determined to be 1.382, 1.374, 1.322, and 1.146 g cm^{-3}, respectively. The significant decrease in density of anGPF3-PDMS might be the consequence of the existence of large voids inside the nanocomposite. As for the electrical conductivity, the incorporation of conductive anGPF aerogels into the PDMS matrix greatly improves the electrical conductivity of the nanocomposites over neat PDMS. Moreover, the electrical conductivity of the nanocomposites increases from anGPF1-PDMS (6.917 S m^{-1}) to anGPF3-PDMS nanocomposite (44.537 S m^{-1}). The increase in electrical conductivity could be attributed to the faster charge transfer through the increased conductive paths in the carbon network, as the junctions and integrity of the cell walls in the porous carbon network are increased from the open cell structure to semi-open cell structure and finally the closed cell structure [18].

To quantify the observed voids in the composites, the void analysis was carefully performed. Weight/volume fraction of the carbon aerogel and volume fraction of the voids are calculated for three different anGPF-PDMS nanocomposites according to the following equations [24]:

$$v_f = \rho_c \cdot \frac{w_f}{\rho_f} \tag{1}$$

$$v_m = \rho_c \cdot \frac{w_m}{\rho_m} \tag{2}$$

$$v_v = 1 - \left(\rho_c \cdot \frac{w_f}{\rho_f} + \rho_c \cdot \frac{w_m}{\rho_m} \right) \tag{3}$$

where w_f and w_m are weight fractions of the filler and matrix, respectively. v_f, v_m and v_c are volume fractions of the filler, matrix and voids, respectively. ρ_f, ρ_m and ρ_c are densities of the filler, matrix and composite, respectively. According to the results (Fig. 2e), it is found that the weight/volume fraction of the filler and the volume fraction of the void increase from anGPF1-PDMS to anGPF3-PDMS. Compared to the small void volume fractions of anGPF1-PDMS (1.031 vol%) and anGPF2-PDMS (4.552 vol%), the value of anGPF3-PDMS is significantly increased to 17.342 vol%, which is around 17 times greater than that of anGPF1-PDMS. It is expected that these voids will weaken the mechanical properties including strength and structural stability.

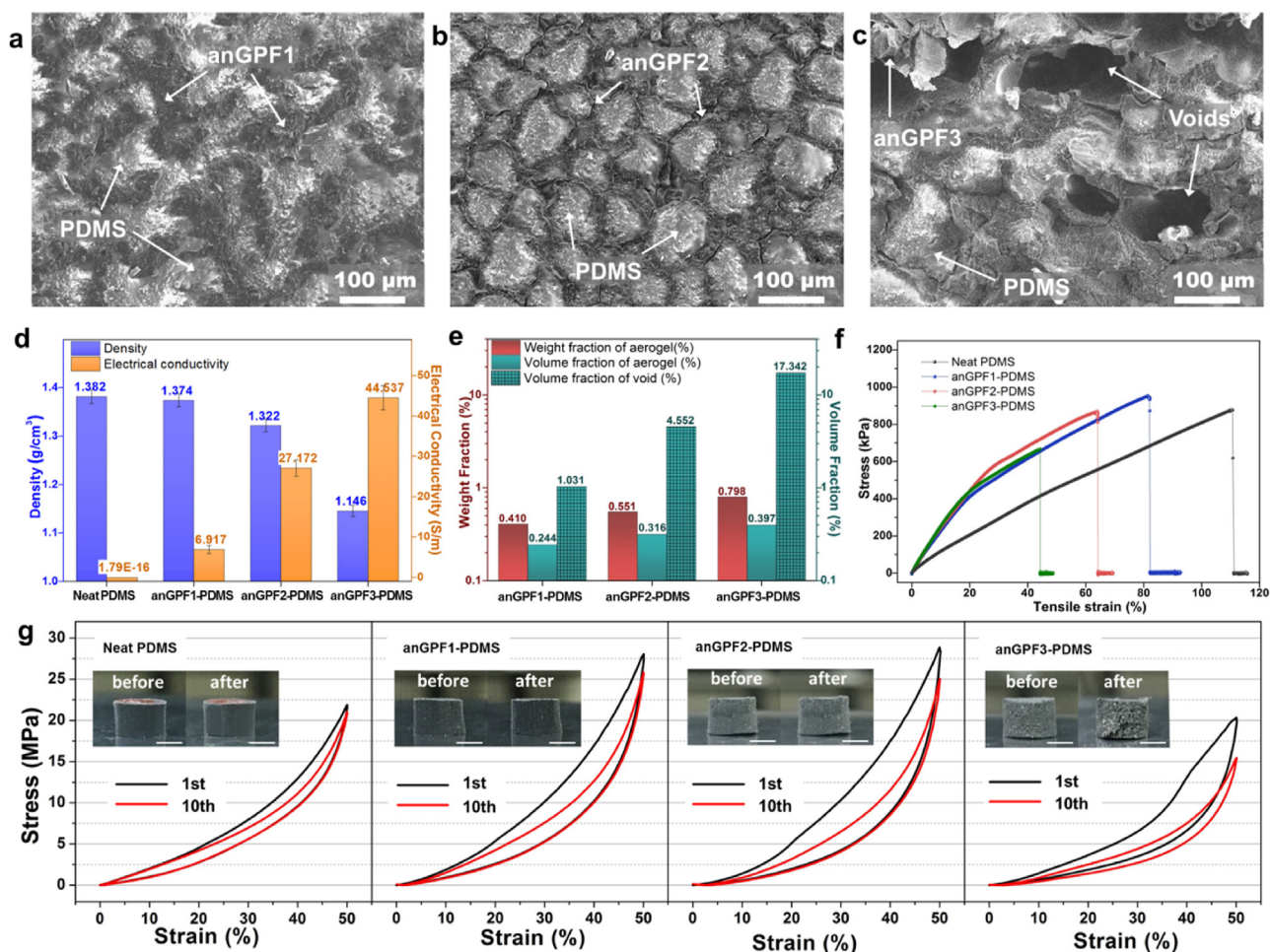Tensile and compression tests were conducted to examine the

Fig. 2. a-c, SEM images of anGPF1-PDMS, anGPF2-PDMS and anGPF3-PDMS. d, Densities and electrical conductivities of neat PDMS, anGPF1-PDMS, anGPF2-PDMS and anGPF3-PDMS, respectively. e, Weight/volume fraction of filler and volume fraction of voids of anGPF1-PDMS, anGPF2-PDMS and anGPF3-PDMS. f-g, mechanical characterization of neat PDMS, anGPF1-PDMS, anGPF2-PDMS and anGPF3-PDMS: f, Stress-strain curves during the tensile testing, g, 10-cycle stress-strain curves during the compressive testing with the inset photographic images showing the samples before and after compression. Scale bar: 2 mm. (A colour version of this figure can be viewed online.)

mechanical properties of anGPF-PDMS nanocomposites reinforced with hierarchical carbon aerogels. The stress-strain curves of neat PDMS and anGPF-PDMS nanocomposites under tensile load (specimen dimension: $30 \times 6 \times 2$ mm^3) are shown in Fig. 2f. Compared to the Young's modulus of neat PDMS (1.248 MPa), the values for anGPF1-PDMS, anGPF2-PDMS and anGPF3-PDMS nanocomposites are substantially increased to 2.438, 2.610 and 2.599 MPa, respectively. While the elongations at break are decreased from neat PDMS (110.6%) to anGPF1-PDMS (81.9%), anGPF2-PDMS (65.0%) and anGPF3-PDMS (43.2%) nanocomposites, which might result from the weak interfacial strength in the composites as well as the increase of voids. It should be noted that although elongations at break decrease for anGPF-PDMS composites, the values are still higher than most of the previously reported porous carbon reinforced PDMS composites (Table S1) [20,21]. Importantly, it is found during tensile test that anGPF1-PDMS and anGPF2-PDMS are demonstrated with much higher tensile strength compared to anGPF3-PDMS (Fig. S4), which could be attributed to their much lower void volume fraction and correspondingly higher structural integrity. In addition to the tensile test, the compression test is also investigated for anGPF-PDMS nanocomposites. Fig. 2g shows the 10-cycle stress−strain curves up to 50% compressive strain for neat PDMS, anGPF1-PDMS, anGPF2-PDMS and anGPF3-PDMS, respectively, with the inset pictures showing the

composites before and after compression (dimension: Φ~4 mm × h~3 mm). The obtained stress−strain curves indicate that the greatest stresses at the first cycle increase from neat PDMS (21.87 MPa) to anGPF1-PDMS (28.03 MPa) and anGPF2-PDMS (28.86 MPa) but decrease at anGPF3-PDMS (20.34 MPa), which might be associated with the undesirably high void contents inside anGPF3-PDMS nanocomposite. Taking advantage of the elastomeric behaviors of PDMS, neat PDMS, anGPF1-PDMS and anGPF2-PDMS are found to be reversible in compressive cyclic loadings, showing their outstanding structural stability. However, expectedly, anGPF3-PDMS fails to keep the structural integrity and stability displaying the appearance of some cracks on the surface of anGPF3-PDMS after the compressions, which is likely the consequence of the voids inside the composites.

It is concluded that the controllable microstructures of the carbon aerogels including hierarchical open, semi-open or closed cell structures will play a critically important role in determining the PDMS composite properties including microstructural morphology, density, electrical conductivity and mechanical properties along with the structural stability. Here, in this study, anGPF-PDMS nanocomposites with the open, semi-open, and closed cell microstructures were further evaluated for both heating and sensing performance to investigate and explore the potential for the use as multifunctional wearable devices.

3.3. Heat-generation performance testing

To evaluate the thermotherapy heating performance of anGPF-PDMS nanocomposites with hierarchical microstructures, the heater devices were assembled using anGPF-PDMS nanocomposites (Fig. 1a). The heating behavior of the nanocomposites (dimension: $20 \times 20 \times 3$ mm^3) without external mechanical stimuli is firstly characterized and investigated. Fig. 3a shows the temperature−time curve of the three anGPF-PDMS nanocomposites based heater devices under five different working voltages. When the voltage is applied, the temperature increases rapidly and then reaches the equilibrium between heat generation and dissipation. It is found that the equilibrium temperature is increased from anGPF1-PDMS to anGPF2-PDMS and anGPF3-PDMS under the same voltage (Table S2). To understand the mechanism underlying the heating behavior, the equilibrium temperatures T_{equ} can be estimated by the following equation [14,25]:

$$T_{equ} = T_0 + \frac{U^2}{RhA} \tag{4}$$

where T_0, U, R, h, A refer to the initial temperature, voltage,

resistance, total heat transfer coefficient and surface area of the heater device, respectively. Therefore, the equilibrium temperature would increase under the same voltage, as the electrical conductivities increase from anGPF1-PDMS to anGPF3-PDMS. To quantify the transduction efficiency of electrical energy to heat energy for anGPF-PDMS nanocomposites based heater devices, the power density (P) is calculated according to the following equation [19,26]:

$$P = \frac{UI}{A} = \frac{I^2 R}{lw} = \frac{U^2}{Rlw} \tag{5}$$

where l and w represent the length and width of the heater device, respectively. Fig. 3b shows the measured equilibrium temperature as a function of the calculated input power density for anGPF-PDMS nanocomposites as well as the previously reported materials (Table S3) [8,9,14−17,19,25−28]. Noticeably, the inverse slope value (power density over temperature, W cm^{-2} °C^{-1}) of anGPF-PDMS nanocomposite is lower than most of the other materials investigated in this study, demonstrating the higher energy transduction efficiency compared to the previously reported works (see more details in Table S3). In addition, anGPF2-PDMS with semi-open cell
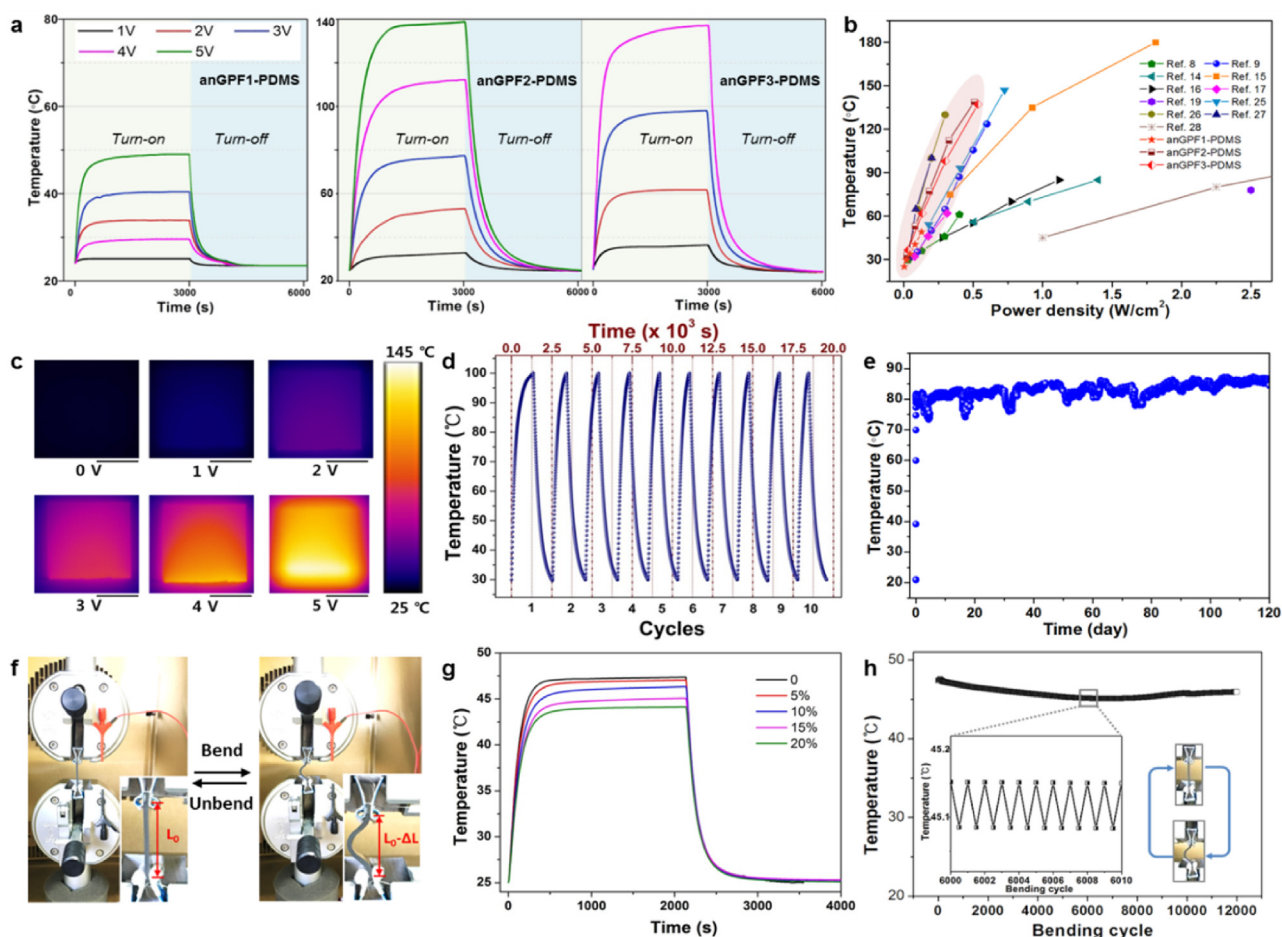

Fig. 3. a, Temperature-time curves of anGPF1-PDMS, anGPF2-PDMS and anGPF3-PDMS based heater devices under different input voltages. b, The measured equilibrium temperature as a function of input power densities for anGPF-PDMS nanocomposites and previously reported materials. c-e, General heating performance of anGPF2-PDMS based heater device without any deformation. c, Infrared camera images showing the temperature distribution with the different input voltage, scale bar: 1 cm. d. Temperature profile of the heater device with cyclic turn on/off of the 4 V voltage. e, Temperature-time curve of the heater device with continuous 3 V input voltage up to 120 days. f-h, Heating performance of anGPF2-PDMS based heater device under bending deformation. f, Experimental set-up for the heat performance testing under bending deformation. g, Temperature-time curves of the heater device under different bending deformations. h, Durability testing of the heater device under cyclic bending-unbending deformation up to 12,000 cycles with continuous 3 V input voltage. Inset: the temperature profile from 6000th to 6010th cycle, showing the ultra-small temperature difference. (A colour version of this figure can be viewed online.)

structure is observed with a lower inverse slope value than anGPF1-PDMS with open cell structure and anGPF3-PDMS with closed cell structure, indicating the highest energy transduction efficiency among the three nanocomposites investigated in this study. Here, the highest energy transduction efficiency of anGPF2-PDMS nanocomposite based heater device could be attributed to the well-defined 3D conductive network in the PDMS matrix, which ensures the uniform and high electrical conductivity throughout the composites material with high structural stability.

Other heating behaviors of anGPF2-PDMS nanocomposites were further characterized which was motivated from the highest energy transduction efficiency. The results are presented in Fig. 3c−h. First, the temperature distributions of the heater device under each applied voltage are monitored with an infrared camera. It can be seen from Fig. 3c that the temperatures are uniformly distributed in each case, especially when the voltages less than 4 V are applied. Besides, the cyclic heating and cooling process with the periodic turn-on/off of the DC voltage (4 V) was also examined, with the starting and ending points set as 30 °C and 100 °C, respectively (Fig. 3d). In the 10th cycle, the device can still reach the temperature as high as the first cycle, indicating the reliable cycling performance. In addition, the long-term stability testing is conducted with the device under continuous 3 V voltage input (Fig. 3e and S6). The impressive finding is that the heating device was able to work continuously even after heating for 120 days and keep to hold a high temperature, clearly indicating the extremely outstanding long-term stability of anGPF2-PDMS, which is an essential parameter to evaluate the performance for a heater device.

To demonstrate the flexibility and the reliability of the heater device, the heating behavior under bending deformations was explored with anGPF2-PDMS (dimensions: $35 \times 25 \times 1.5$ mm^3). The testing set-up is shown in Fig. 3f. The length between two grips is labeled as L_0 and the bending deformations are defined as the percentage change of the length over L_0 ($\Delta L/L_0 \times 100\%$). Fig. 3g shows the temperature−time curves of the heater device under different bending deformations (0%-unbend state, 5%, 10%, 15%, 20%) with 3 V input voltage. Following the increase of the bending deformations, the equilibrium temperatures are found to decrease, with the values (T_{bend}) at 5%, 10%, 15%, and 20% bending deformations recorded to be 47.04, 46.34, 45.07, and 44.12 °C, respectively. Therefore, even at 20% bending deformation, the device can still maintain 93.16% of the temperature compared to the unbend state, demonstrating the excellent stability of the heater device under large bending deformations (Fig. S7). It might be worth noting that on top of the temperature change, the resistance of the device was also varied in response to the bending deformations which could be further exploited for the use as a stimuli-responsive sensor. Moreover, the heat-generation performance was further investigated under cyclic bending-unbending deformations with 3 V input voltage to evaluate the durability of the heating device (Fig. 3h). It is surprising to observe that the device can still keep the high temperature even after being bent for 12,000 cycles at 5% deformation, and the temperature difference between each cycle is measured to be only less than 0.1 °C, ensuring the extremely high durability of the device under cyclic deformation [27]. Therefore, anGPF2-PDMS based heater device is demonstrated with an excellent combination of the efficient energy transduction as well as the outstanding stability and durability under external deformations. This blend of exceptionally outstanding features of anGPF2-PDMS nanocomposite could be attributed to the semi-open cell structure of the porous anGPF2 aerogel, which can provide the effective pathway for PDMS fluid to penetrate inside the porous structure of the aerogel, thereby contributing to the formation of the well-defined conductive network inside the composite along with the high structural stability.

3.4. Stimuli-responsive sensing testing

Given that the resistance of the device can change in response to the applied mechanical stimuli, anGPF-PDMS nanocomposites with hierarchical microstructures were further investigated and explored for the potential use as stimuli-responsive sensors. The relative resistance changes, $\Delta R/R_0$ (%), were monitored and analyzed under different mechanical deformations to evaluate the responsiveness and sensitivity of the devices as a stimuli-responsive sensor. First, the relative resistance change as a function of uniaxial tensile strain up to elongation at break was investigated for anGPF1-PDMS, anGPF2-PDMS and anGPF3-PDMS, respectively (sample dimension: $30 \times 6 \times 2$ mm^3). As shown in Fig. 4a, the change in the relative resistance increases as the tensile strain increases for all the three anGPF-PDMS nanocomposites. To evaluate the sensitivity of the sensor device under tensile deformation, the gauge factor (GF) is obtained based on the linear fitting of the following equation [29]:

$$\frac{\Delta R}{R_0} = GF \cdot \varepsilon \tag{6}$$

where ε is the tensile strain. It was observed that the GF values of anGPF-PDMS nanocomposites are highly dependent on the strain region, and the values before the elongation at break of anGPF1-PDMS (~81.9%), anGPF2-PDMS (~65.0%) and anGPF3-PDMS (~43.2%) are determined to be 369.03, 290.60 and 57.14, respectively, indicating the outstanding combination of high sensitivity and large elongation at break compared to the porous material based composite sensors reported previously (Table S1). In addition, the GF values in the initial linear region (strain: 0−20%) of anGPF1-PDMS, anGPF2-PDMS and anGPF3-PDMS are estimated to be 2.64, 0.52 and 2.25, respectively, indicating the highest sensitivity with anGPF1-PDMS but the lowest with anGPF2-PDMS among the three nanocomposites.

To evaluate the repeatability and stability of the sensor devices, the changes in the relative resistance of anGPF-PDMS nanocomposites are recorded under cyclic loading-unloading of 20% tensile strain (Fig. 4b). The amplitudes of the change in the relative resistance seem to remain almost constant for the three anGPF-PDMS nanocomposites, indicating the high stability of anGPF-PDMS nanocomposites under the cyclic triangular input tensile deformation. In addition, the resistance curves (output) are substantially consistent with the cyclic tensile deformations (input), showing a triangular waveform with fast responsiveness. The repeatability and stability of the devices are further investigated under the tensile deformation with square waveform (Fig. 4c), where the composites would be held for 60 s at both 20% and 0% strains after the loading and unloading process, respectively. The important finding here is that the changes in the relative resistance are observed with outstanding repeatability without any compromise for anGPF1-PDMS and anGPF2-PDMS. The relative resistance change−time curve is also observed to be a square waveform just similar to the change of the applied deformation, indicating their outstanding stability and excellent repeatability under the cyclic square input in tension mode. However, the resistance curve of anGPF3-PDMS was found to fail to follow up the corresponding strain curve, showing poor repeatability of anGPF3-PDMS under the cyclic tensile deformation.

The sensing performance is further investigated under the compressive load up to 70% strain for anGPF-PDMS nanocomposites (dimension: Φ~4 mm × h~3 mm, Fig. 4d). The relative resistance change of anGPF1-PDMS and anGPF2-PDMS increases linearly up to around 20% strain followed by the exponential increase up to 70% strain, evidenced by the dramatic increase of GF
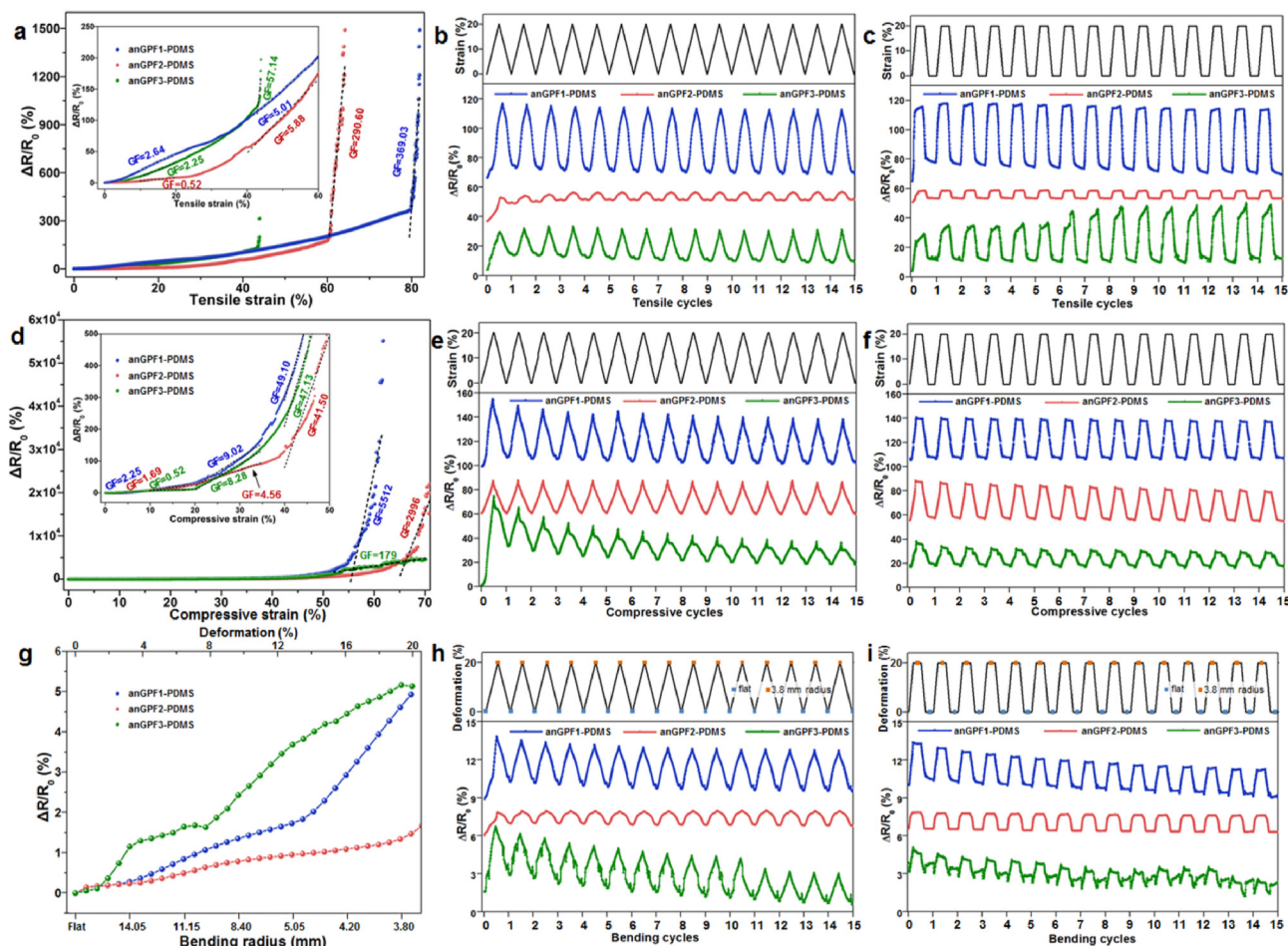
Fig. 4. Stimuli-responsive sensing performance of anGPF1-PDMS, anGPF2-PDMS and anGPF3-PDMS based sensor devices under tensile (a−c), compressive (d−f) and bending (g−i) deformations. a, Relative resistance change as a function of tensile strain up to elongations at break. b and c, Relative resistance change under 20% cyclic tensile strain with the triangular (b) and square waveform (c), respectively. d, Relative resistance change as a function of compressive strain. e and f, Relative resistance change under 20% cyclic compressive strain with the triangular (e) and square waveform (f), respectively. g, Relative resistance change as a function of bending deformation. h and i, Relative resistance change under 20% cyclic bending deformation with the triangular (h) and square waveform (i), respectively. (A colour version of this figure can be viewed online.)

values (from 2.25 to 5512 for anGPF1-PDMS, from 1.69 to 2996 for anGPF2-PDMS). The increase of *GF* value of anGPF1-PDMS is higher than that of anGPF2-PDMS under the same compressive strain, indicating the higher sensitivity of anGPF1-PDMS under compressive loading. However, the change in the relative resistance of anGPF3-PDMS shows a gradual increase after 50% strain (*GF* of 179), which could be related to the structural failure of anGPF3-PDMS at such high compressive strain. The stability and repeatability of the devices under cyclic loading-unloading (triangular input) and cyclic loading-holding-unloading-holding (square input) compressive deformation are also characterized and the results are shown in Fig. 4e and f. Similar to the cyclic tensile deformation, anGPF1-PDMS and anGPF2-PDMS are observed with the outstanding stability and excellent repeatability during the cyclic compressive deformation. The changes in the relative resistance of anGPF1-PDMS and anGPF2-PDMS are pretty well-followed up the strain curves under both cyclic modes. However, the stability and repeatability are not observed for anGPF3-PDMS, especially under the cyclic triangular input compressive deformation. The amplitudes of the relative resistance change decrease as the number of cycles increase, and the resistance curve of anGPF3-PDMS seems not to correspond well with the strain curve. Similar findings are also observed for anGPF-PDMS nanocomposites under bending

deformations (sample dimension: $30 \times 6 \times 2$ mm^3, Fig. 4g−i). The bending deformation is defined as the percentage change of length over initial length ($\Delta L/L_0 \times 100\%$), and the corresponding bending radius is also calculated. It is observed that anGPF1-PDMS and anGPF2-PDMS can show the outstanding stability and repeatability while anGPF3-PDMS failed to exhibit the repeatability under cyclic bending deformation.

Therefore, this investigation can conclude that anGPF1-PDMS with open-cell structure is observed with the highest sensitivity and relatively good repeatability compared to anGPF2-PDMS and anGPF3-PDMS. This is probably because the non-continuous open cell structure of anGPF1 is expected to have more disconnection under the external mechanical deformations, making anGPF1-PDMS more sensitive to the breakage of the conductive path in the carbon network [21]. anGPF2-PDMS reinforced with semi-open cell carbon aerogel is observed with the relatively high sensitivity and outstanding repeatability without any noticeable compromise, thanks to the high structural integrity and well-defined cellular conductive network inside the composite. However, anGPF3-PDMS with closed cell structure failed to exhibit the repeatability under the cyclic deformation, resulting from the large volume fraction of voids in the composites and the poor structural stability.

3.5. Wearability testing

To evaluate and demonstrate the practical application potential of anGPF-PDMS nanocomposites as multifunctional wearable devices, anGPF2-PDMS based heater/sensor device with the dimension of $35 \times 25 \times 1.5$ mm^3 is placed on the wrist (Fig. 5a) and under the heel (Fig. 5d), serving as a heater and a stimuli-responsive sensor, respectively. For this investigation, anGPF2-PDMS is selected because the composite is found to have the highest energy transduction efficiency and the relatively high sensitivity along with outstanding repeatability without any noticeable compromise. As shown in Fig. 5b, the surface temperature of the device on the wrist is monitored to be around 48 °C under 3 V with a uniform temperature distribution, where the surface temperature of the human skin is measured to be around 32 °C. The temperature difference is found to be quite moderate and uniform enough for the device to work as a wearable thermotherapy device. Moreover, the surface temperature of the device can be readily controlled by adjusting the input voltage. In addition, the functionality of the device as a stimuli-responsive sensor is also evaluated by recording the relative resistance change during the body joint movement. Fig. 5c shows the relative resistance change of the device as a function of time during the up and down movements of the human wrist. Basically, the resistance is measured to increase as the wrist bends upward or downward, and then recover to the initial value as the wrist comes back to the horizontal position. So, in addition to the heater device, the composite can also work as a wearable stimuli-responsive sensor to monitor the movement of human body joints.

The multifunctionality and the wearability of the device are also confirmed by applying the device under the heel. Similarly, the surface temperature is observed to be around 48 °C with a uniform temperature distribution when 3 V is applied (Fig. 5e). Moreover, the resistance responsiveness of the device under the heel with three different movement modes is also investigated (Fig. 5f). The interesting observation is that the three modes can be clearly distinguishable among regular walking, standing, and skipping based on the relative resistance change–time curves. Compared to the skipping mode, the smaller frequency of the resistance change along with more stable peak values of the relative resistance

change is observed in the regular walking mode, while the standing mode shows a slow decrease of resistance very likely due to the stress relaxation. Once again, the uniform temperature distribution and the structural stability during the movement of wrist or heel could be explained by the well-defined conductive network in PDMS matrix and the high structural integrity of anGPF2-PDMS nanocomposite, benefiting from the effective penetration of PDMS polymer fluids throughout the semi-open cell structure of the carbon aerogel. Therefore, anGPF2-PDMS based heater/sensor device is demonstrated with great promise for its practical application as a multifunctional wearable device, in which the thermotherapy heating and stimuli-responsive sensing can be synergistically worked.

4. Conclusions

3D conductive anGPF aerogels reinforced PDMS nanocomposites were developed for the multifunctional wearable devices in this study. The microstructures of anGPF aerogels can be effectively controlled by varying the GO loading fractions, showing the hierarchical open, semi-open or closed cell structures. It is found that the microstructures of carbon aerogels can play a crucial role in determining the composite properties including structural morphology, density, electrical conductivity and mechanical properties. As a thermotherapy heater, the equilibrium temperature increases from anGPF1-PDMS to anGPF3-PDMS under the same voltage, due to the increase of the electrical conductivity. Besides, anGPF2-PDMS with semi-open cell structure is observed with the highest energy transduction efficiency compared to anGPF1-PDMS and anGPF3-PDMS, benefiting from the well-defined conductive network and the high structural stability, The extremely long-term stability was also confirmed for anGPF2-PDMS based heater device by the continuous heating for at least 120 days. More importantly, the anGPF2-PDMS based heater device is also demonstrated with the excellent flexibility and outstanding durability by the stable heating performance under the cyclic bending deformation for more than 12,000 cycles. As a stimuli-responsive sensor, anGPF-PDMS nanocomposites exhibit the extraordinary combination of high sensitivity (0.52–369.03) and large elongation at break (43.2%–81.9%). Moreover, anGPF1-PDMS
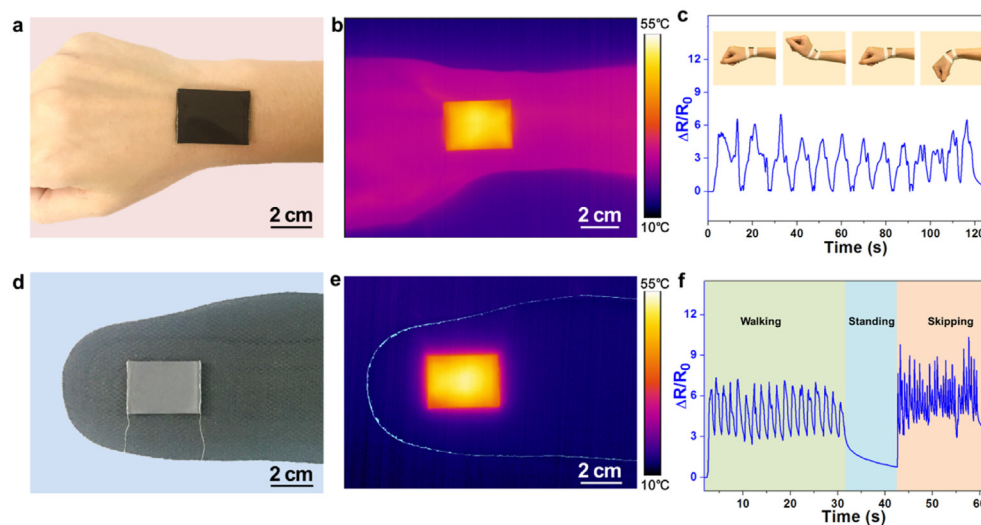

Fig. 5. Wearability testing of anGPF2-PDMS based multifunctional device. a, Photographic image showing the device worn on the wrist. b, Infrared images of the heater device on the wrist with 3 V input voltage. c, Relative resistance change monitored by the device during the bending and unbending of the wrist. d, Photographic image showing the device worn on the shoe-pad. e, Infrared images of the heater device on the shoe-pad with 3 V input voltage. f, Relative resistance change monitored by the device under the heel during the different movement states. (A colour version of this figure can be viewed online.)

and anGPF2-PDMS reinforced by open cell and semi-open cell aerogels are observed with relatively high sensitivity and excellent repeatability during the cyclic deformations due to their high structural integrity. While anGPF3-PDMS with closed cell structure failed to exhibit the repeatability under the cyclic deformation, resulted from the high volume fraction of voids and poor structural stability. Finally, the wearability and feasibility of anGPF-PDMS nanocomposites to use as a practical wearable device was further verified by anGPF2-PDMS with the uniform temperature distribution and the reliable body motion detecting performance. In summary, by controlling and optimizing the microstructures of the porous carbon aerogels, anGPF2-PDMS nanocomposites with tailored semi-open cell structure are demonstrated with great potential for its application as a multifunctional wearable heater and sensor device. It could provide a new solution to develop a multifunctional heater/sensor device with robust structural reliability as well as desirable wearable performances.

CRediT authorship contribution statement

Yan Sun: Methodology, Investigation, Writing - original draft, Writing - review & editing. **Deping Li:** Methodology. **Jong Uk Kim:** Resources. **Bing Li:** Resources, Investigation. **Seung-Hyun Cho:** Resources. **Tae-il Kim:** Resources. **Jae-Do Nam:** Resources. **Lijie Ci:** Resources. **Jonghwan Suhr:** Writing - review & editing, Funding acquisition, Project administration, Supervision.

Declaration of competing interest

The authors declare that they have no known competing financial interests or personal relationships that could have appeared to influence the work reported in this paper.

Acknowledgements

Appendix A. Supplementary data

Supplementary data to this article can be found online at https://doi.org/10.1016/j.carbon.2020.09.073.

References

[1] D. Son, J. Lee, S. Qiao, R. Ghaffari, J. Kim, J.E. Lee, et al., Multifunctional wearable devices for diagnosis and therapy of movement disorders, Nat. Nanotechnol. 9 (5) (2014) 397–404.
[2] X. Wang, Z. Liu, T. Zhang, Flexible sensing electronics for wearable/attachable health monitoring, Small 13 (25) (2017) 1–19.
[3] Yeo JC. Kenry, C.T. Lim, Emerging flexible and wearable physical sensing platforms for healthcare and biomedical applications, Microsyst. Nanoeng. 2 (1) (2016) 1–19.
[4] N.S. Jang, K.H. Kim, S.H. Ha, S.H. Jung, H.M. Lee, J.M. Kim, Simple approach to high-performance stretchable heaters based on kirigami patterning of conductive paper for wearable thermotherapy applications, ACS Appl. Mater. Interfaces 9 (23) (2017) 19612–19621.
[5] Y. Wang, Z. Yu, G. Mao, Y. Liu, G. Liu, J. Shang, et al., Printable liquid-metal@ PDMS stretchable heater with high stretchability and dynamic stability for wearable thermotherapy, Adv. Mater. Tech. 4 (2) (2019), 1800435.
[6] Y. Khan, A.E. Ostfeld, C.M. Lochner, A. Pierre, A.C. Arias, Monitoring of vital signs with flexible and wearable medical devices, Adv. Mater. 28 (22) (2016) 4373–4395.
[7] K. Takei, W. Honda, S. Harada, T. Arie, S. Akita, Toward flexible and wearable human-interactive health-monitoring devices, Adv. Healthc. Mater. 4 (4) (2015) 487–500.
[8] Y.Q. Li, W.B. Zhu, X.G. Yu, P. Huang, S.Y. Fu, N. Hu, et al., Multifunctional wearable device based on flexible and conductive carbon sponge/polydimethylsiloxane composite, ACS Appl. Mater. Interfaces 8 (48) (2016) 33189–33196.
[9] Q. Zhang, Y. Yu, K. Yang, B. Zhang, K. Zhao, G. Xiong, et al., Mechanically robust and electrically conductive graphene-paper/glass-fibers/epoxy composites for stimuli-responsive sensors and Joule heating deicers, Carbon 124 (2017) 296–307.
[10] A.J. Bandodkar, I. Jeerapan, J. Wang, Wearable chemical sensors: present challenges and future prospects, ACS Sens. 1 (5) (2016) 464–482.
[11] S. Choi, H. Lee, R. Ghaffari, T. Hyeon, D.H. Kim, Recent advances in flexible and stretchable bio-electronic devices integrated with nanomaterials, Adv. Mater. 28 (22) (2016) 4203–4218.
[12] T.Q. Trung, N.E. Lee, Recent progress on stretchable electronic devices with intrinsically stretchable components, Adv. Mater. 29 (3) (2017) 1–29.
[13] T.Q. Trung, N.E. Lee, Flexible and stretchable physical sensor integrated platforms for wearable human-activity monitoringand personal healthcare, Adv. Mater. 28 (22) (2016) 4338–4372.
[14] S. Hong, H. Lee, J. Lee, J. Kwon, S. Han, Y.D. Suh, et al., Highly stretchable and transparent metal nanowire heater for wearable electronics applications, Adv. Mater. 27 (32) (2015) 4744–4751.
[15] B.W. An, E.J. Gwak, K. Kim, Y.C. Kim, J. Jang, J.Y. Kim, et al., Stretchable, transparent electrodes as wearable heaters using nanotrough networks of metallic glasses with superior mechanical properties and thermal stability, Nano Lett. 16 (1) (2016) 471–478.
[16] M. Cao, M. Wang, L. Li, H. Qiu, Z. Yang, Effect of graphene-EC on Ag NW-based transparent film heaters: optimizing the stability and heat dispersion of films, ACS Appl. Mater. Interfaces 10 (1) (2018) 1077–1083.
[17] S. Choi, J. Park, W. Hyun, J. Kim, J. Kim, Y.B. Lee, et al., Stretchable heater using ligand-exchanged silver nanowire nanocomposite for wearable articular thermotherapy, ACS Nano 9 (6) (2015) 6626–6633.
[18] A. Idowu, B. Boesl, A. Agarwal, 3D graphene foam-reinforced polymer composites – a review, Carbon 135 (2018) 52–71.
[19] J. Bustillos, C. Zhang, B. Boesl, A. Agarwal, Three-dimensional graphene foam-polymer composite with superior deicing efficiency and strength, ACS Appl. Mater. Interfaces 10 (5) (2018) 5022–5029.
[20] Y. Pang, H. Tian, L. Tao, Y. Li, X. Wang, N. Deng, et al., Flexible, highly sensitive, and wearable pressure and strain sensors with graphene porous network structure, ACS Appl. Mater. Interfaces 8 (2016) 26458–26462.
[21] S. Wu, R.B. Ladani, J. Zhang, K. Ghorbani, X. Zhang, A.P. Mouritz, et al., Strain sensors with adjustable sensitivity by tailoring the microstructure of graphene aerogel/PDMS nanocomposites, ACS Appl. Mater. Interfaces 8 (37) (2016) 24853–24861.
[22] Y. Sun, L. Chen, J. Yu, B. Yoon, S.K. Lee, J.-D. Nam, et al., Lightweight graphene oxide-based sponges with high compressibility and durability for dye adsorption, Carbon 160 (2020) 54–63.
[23] Y. Sun, M.-K. Kim, M. Wang, J. Yu, S.Y. Hong, J.-D. Nam, et al., Bio-inspired multiple-stimuli responsive porous materials with switchable flexibility and programmable shape morphing capability, Carbon 161 (2020) 702–711.
[24] R.F. Gibson, Principles of Composite Material Mechanics, CRC press, 2011.
[25] Y. Cheng, H. Zhang, R. Wang, X. Wang, H. Zhai, T. Wang, et al., Highly stretchable and conductive copper nanowire based fibers with hierarchical structure for wearable heaters, ACS Appl. Mater. Interfaces 8 (48) (2016) 32925–32933.
[26] J. Kang, Y. Jang, Y. Kim, S.H. Cho, J. Suhr, B.H. Hong, et al., An Ag-grid/graphene hybrid structure for large-scale, transparent, flexible heaters, Nanoscale 7 (15) (2015) 6567–6573.
[27] J. Kang, H. Kim, K.S. Kim, S.K. Lee, S. Bae, J.H. Ahn, et al., High-performance graphene-based transparent flexible heaters, Nano Lett. 11 (12) (2011) 5154–5158.
[28] A.R. Raji, T. Varadhachary, K. Nan, T. Wang, J. Lin, Y. Ji, et al., Composites of graphene nanoribbon stacks and epoxy for joule heating and deicing of surfaces, ACS Appl. Mater. Interfaces 8 (5) (2016) 3551–3556.
[29] M. Amjadi, K.-U. Kyung, I. Park, M. Sitti, Stretchable, skin-mountable, and wearable strain sensors and their potential applications: a review, Adv. Funct. Mater. 26 (11) (2016) 1678–1698.